Version of Record at: https://doi.org/10.1063/5.0211922

Physics of Plasmas

RESEARCH ARTICLE | AUGUST 22 2024

Self-generated magnetic fields in the hot spot of direct-drive cryogenic implosions at Omega

C. A. Frank ; A. Bose

Check for updates

Phys. Plasmas 31, 082709 (2024)
https://doi.org/10.1063/5.0211922

View Online
Export Citation

Physics of Plasmas
Special Topic:
Celebrating the Contributions of Emeritus Professor Robert (Bob) Dewar
Guest Editors: Adelle Wright, Amitava Bhattacharjee and Phil Morrison
Submit Today!
AIP Publishing

AIP Publishing

Version of Record at: https://doi.org/10.1063/5.0211922

Physics of Plasmas ARTICLE pubs.aip.org/aip/pop

Self-generated magnetic fields in the hot spot of direct-drive cryogenic implosions at Omega

Cite as: Phys. Plasmas **31**, 082709 (2024); doi: 10.1063/5.0211922
Submitted: 2 April 2024 · Accepted: 1 August 2024 ·
Published Online: 22 August 2024

View Online Export Citation CrossMark

C. A. Frank and A. Bose[a)]

AFFILIATIONS

Department of Physics and Astronomy, University of Delaware, Newark, Delaware 19716-2570, USA

[a)]Author to whom correspondence should be addressed: bose@udel.edu

ABSTRACT

This work reports that Biermann self-generated magnetic fields of ≈ 200 MG and Hall parameters of ≈ 1.5 are produced in the stagnation phase of direct-drive cryogenic implosions at Omega. The magnetic fields produce a drop of 2.4% in fusion yield and 1% in ion temperature. A quantitative estimate of the effect of self-generated magnetic fields on yield and ion temperature is essential, since direct measurements of these fields are not available. Reconstructed simulations of the 50 Gbar implosions, with all the stagnation measurements reproduced simultaneously by a combination of mid- and low-mode asymmetries as degradation mechanisms [Bose *et al.*, Phys. Plasmas **25**, 062701 (2018)], are used to obtain the estimates. The magnetic fields cause a decrease in yield due to the Righi–Leduc heat flow, which exceeds any benefits from heat flow suppression due to magnetization. It is important to note that both direct-drive Omega-scale implosions and indirect-drive National Ignition Facility (NIF)-scale implosions [Walsh *et al.*, Phys. Rev. Lett. **118**, 155001 (2017)] produce similar estimates for the magnetic field strength, and both show a decrease in fusion yield, with the Righi–Leduc transport as the loss mechanism. However, the yield degradation at Omega is small and lower by ≈ 5× compared to the indirect-drive ignition-scale NIF estimate.

© 2024 Author(s). All article content, except where otherwise noted, is licensed under a Creative Commons Attribution (CC BY) license (https://creativecommons.org/licenses/by/4.0/). https://doi.org/10.1063/5.0211922

I. INTRODUCTION

During the deceleration phase of inertial confinement fusion (ICF) implosions, the interface between the hot spot (with $T_i \approx 3$–5 keV and $\rho \approx 50$ g/cc) and the cold and dense shell (with ion temperature $T_i \approx 0.25$–1 keV and density $\rho \approx 100$–150 g/cc) is susceptible to the Rayleigh–Taylor instability (RTI).[1–6] The RTI produces spikes and bubbles that distort the hot spot, decreasing the fusion yield. For nonlinear RTI, mass ablation introduces flows and vorticity within the bubbles, causing pressure gradients $\nabla P \sim \text{Mach}^2$ (Ref. 7) at the edge of the hot spot. The RTI distortions introduce a nonzero curl to the ratio of the pressure gradient to the density, $\nabla \times (\nabla P_e/n_e)$, giving rise to Biermann self-generating magnetic fields.

Measurements of self-generated magnetic fields in the hot spot of ICF implosions and measurements of the corresponding effects on stagnation observables are currently unavailable. This is primarily because the surrounding dense shell is typically opaque to charged particle radiography and to Faraday rotation measurements. However, the fact that magnetic fields are generated in implosions was confirmed from radiography of the outer surface of direct-drive spherical implosions. The measured electric and magnetic fields at the outer surface were used to conjecture self-generated magnetic fields at the inner fuel–shell interface during stagnation.[8–10] Self-generated Biermann magnetic fields were measured directly in laser-irradiated planar foil experiments.[11,12] These fields, generated via the RTI, were of ∼1 MG magnitude, and approached values significant enough to magnetize the plasma and inhibit thermal transport.[12] For direct-drive implosions, self-generated magnetic fields of ≈3 MG on the outer surface of the capsule were measured using proton radiography during the laser drive phase.[13] These fields were produced from the pre-imposed outer surface defects, including glue spot and stalk and were analyzed using *DRACO* simulations.[13] However, for direct-drive cryogenic Omega implosions, no measurements or simulations of deceleration-phase self-generated magnetic fields have been made.

For parameters relevant to the hot spot of indirect-drive National Ignition Facility (NIF) implosions, two-dimensional planar magnetohydrodynamic (MHD) simulations estimated the generation of fields during the stagnation phase of ∼10–50 MG.[14,15] Fields of this magnitude were found to correspond to Hall parameters $\omega_e \tau_e > 1$, indicating that magnetization could potentially suppress heat transport within the hot spot.[14,15] Magnetic fields of the order of ∼50 MG, corresponding to heat-loss suppression by >5%, were estimated in the hot spot of NIF implosions by post-processing (xRAGE,

© Author(s) 2024

Version of Record at: https://doi.org/10.1063/5.0211922

hydrodynamic only) simulations.[16] However, the aforementioned simulations and calculations either did not dynamically account for the hot spot compression or did not concurrently include the effects of self-generated magnetic fields on the fusion yield and thermal transport in the simulation. Recently, MHD simulations of NIF indirect-drive implosions including the effects of self-generated magnetic fields using the code *Gorgon* showed fields of the order of ∼100 MG, with corresponding $\omega_e\tau_e \sim 3$ produced at the interface of the hot spot and shell at stagnation.[17] Typically, one would expect that magnetization of the plasma at the edge of the hot spot would suppress heat losses to the surrounding cold shell and boost the fusion yield and temperature.[16,18] However, counterintuitively, these simulations showed a degradation in yield of 11.6% and a decrease in ion temperature of 2.5% for the NIF-scale implosions approaching the ignition cliff. An explanation for this in terms of the Righi–Leduc transport was provided in Ref. 17; this effect has been further investigated in the context of Omega implosions in this paper.

This paper is the first to investigate the effect of self-generated magnetic fields in the hot spot for direct-drive cryogenic implosions at Omega. The key questions addressed in this paper are: How large are the hot spot self-generated magnetic fields and Hall parameter ($\omega_e\tau_e$) for direct-drive Omega implosions? What effect do these fields have on the fusion yield and ion temperature? Essential differences between direct-drive Omega and indirect-drive NIF implosions that necessitates this analysis are listed as follows: (1) Unlike the indirect-drive NIF implosions, for direct-drive with Omega 60, mid-mode perturbations[19] (particularly the Legendre mode $\ell = 10$ in addition to other mid-modes) are seeded due to the superposition of the 60 laser beams at Omega.[20] These beam modes are amplified by cross-beam energy transfer[20,21] and imprint the imploding capsule. The beam modes then feed through to the inner surface of the shell and seed the deceleration-phase RTI. (2) Unlike at ignition-scale NIF, there is no alpha heating in sub-ignition Omega-scale implosions. Therefore, in contrast to the previous NIF-scale simulations,[17] where the effect of alpha heating and the role of magnetic fields were not separated, in the sub-ignition Omega implosions the effect of magnetization needs to be decoupled from alpha heating. (3) Additionally, the Omega implosions are smaller in target radius and implosion times (by a factor of $\approx 4\times$) relative to the NIF implosions. This difference in the hot spot size and the duration of the deceleration phase calls for an estimation of the scaled self-generated magnetic field and effects on yield for Omega-scale implosions.

In order to address the above questions and obtain realistic estimates pertaining to Omega implosions, we consider an ensemble of cryogenic implosions that are repeatable with little shot-to-shot variations, and have been analyzed extensively using multidimensional simulations, with the data on stagnation observables made available in prior publications. We use the 50 Gbar implosions, which are cryogenic implosions producing fuel hot spot pressure exceeding 50 Gbar.[22,23] A summary of the stagnation observable for these shots can be found in Table I of Ref. 19. The analysis procedure discussed in Ref. 19 (see Fig. 3) involves first simulating the laser drive using a 1D code, then introducing *ad hoc* perturbations to seed the deceleration-phase RTI for a 2D simulation of the deceleration phase. Two categories of degradation were considered: (1) low modes ($\ell \leq 6$), which can originate from target positioning and laser beam balance, and (2) mid-modes ($6 < \ell < 40$), which can originate from the laser beam superposition (higher modes are ablatively stabilized; see Fig. 1 of Ref. 7). Low modes degrade the fusion yield by producing a drop in the hot spot pressure[7] due to increased residual kinetic energy.[24] The mid-modes cause a degradation in yield via a drop in the fusion volume[7] because the cold RTI bubbles do not sustain fusion. Using a combination of the low and mid-modes, all the stagnation observables for the 50 Gbar implosion were reconstructed in Ref. 19. This work extends the same analysis method, now with the addition of hot spot self-generated magnetic fields, to estimate the effect of the fields on the fusion yield and ion temperature.

This paper is structured as follows: In Sec. II, the analysis technique using the code *DEC2D* to simulate the deceleration phase of Omega implosions is discussed and the MHD solvers incorporated in *DEC2D* are outlined. In Sec. III, the effect of magnetic fields on the implosion dynamics, fusion yield, and temperature are shown for the direct-drive Omega implosions.

II. METHODS

The Omega implosion used for this analysis is the high-yield shot 77 068 from the 50 Gbar campaign.[7,19,22] The pulse shape and target dimensions are shown in Fig. 1. The laser-drive (or acceleration) phase is simulated using the 1D code *LILAC*,[25] with the laser deposition models optimized previously to reproduce in-flight observables such as laser-energy deposition and shell trajectory.[26,27] The hydrodynamic profiles of the in-flight target are extracted from *LILAC* at the end of the laser-drive to initialize the deceleration-phase simulation using the code *DEC2D*.

DEC2D is an Eulerian moving-mesh code used to simulate the deceleration phase of ICF implosions.[24,28,29] This code includes models for thermal-transport and multi-group radiation transport. *DEC2D* has been benchmarked with *LILAC*[23] and has been validated through extensive comparison with RTI theory growth rates and ICF deceleration-phase theory[3,4,6] and through comparison with experimental observables.[19] Detailed description of this code, the thermal transport, and the radiation transport models included can be found in Refs. 30 and 31.

Velocity perturbations, in 2D, are added to the inner surface of the shell to seed the deceleration-phase RTI for the *DEC2D* simulations.[30] The perturbations are characterized by their Legendre mode number ℓ. Analogous to Ref. 19, a low-mode case, a mid-mode case, and a combination spectrum of modes shown in Fig. 2 used to

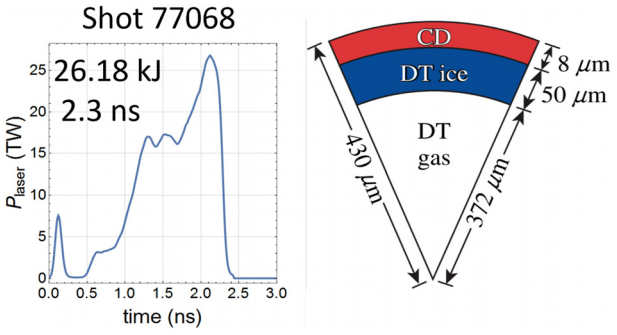

FIG. 1. The laser pulse and target for the Omega shot 77 068 (one of the "50 Gbar" shots) used in this analysis. Reproduced with permission from Bose *et al.*, Phys. Plasmas **25**, 062701 (2018). Copyright 2018 AIP Publishing.

© Author(s) 2024

Version of Record at: https://doi.org/10.1063/5.0211922

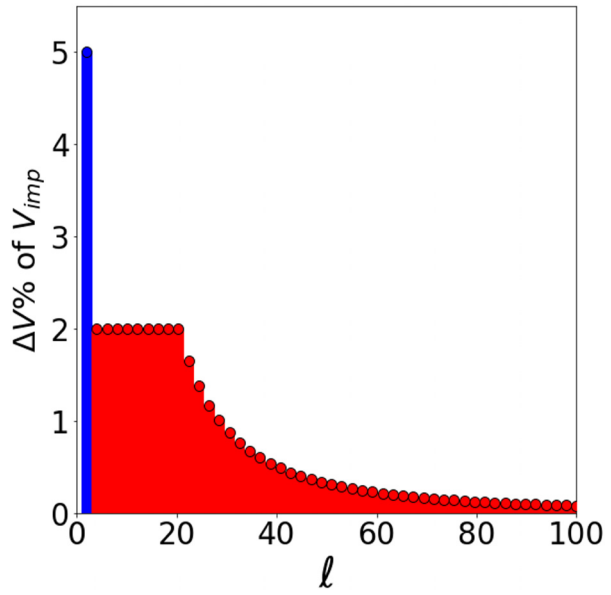

FIG. 2. The multi-mode velocity perturbation spectra $\Delta V/V_{imp}$ % (as a percent of the implosion velocity) that were used in *DEC2D* simulations to seed the deceleration-phase RTI in order to reconstruct the stagnation observables for the 50 Gbar experiments (particularly the shot 77 068). The multi-mode spectra consist of an $\ell = 2$ at 5% (in blue), mid-modes $\ell \leq 20$ at 2% (red), and a $1/\ell^2$ roll-over spectrum of higher modes $20 \leq \ell \leq 100$ (red). The latter is motivated by the DT-ice inner surface roughness spectrum. Reproduced with permission from Bose *et al.*, Phys. Plasmas **25**, 062701 (2018). Copyright 2018 AIP Publishing.

reproduce the stagnation observables for the 50 Gbar implosions are used in this analysis. The yield for the reconstructed simulation is 5.3×10^{13}, matching the experimentally observed yield for shot 77 068. This was obtained by degrading the 1D (clean) yield from 1.7×10^{14} in order to match the experiments (i.e., a yield-over-clean, YOC = 0.32). The reconstructed simulation also matches all stagnation observables from the experiment; these are listed in Table II of Ref. 19. The single mode $\ell = 2$ is used to represent low modes and the mode $\ell = 10^*$ is used to represent mid-modes. As in Ref. 7, the $\ell = 10*$ case includes sideband modes, i.e., perturbations at $\ell = 8$ and $\ell = 12$ with a smaller amplitude (20% of the dominant $\ell = 10$). The YOC for the $\ell = 2$ and the $\ell = 10*$ simulations used in the analysis is 0.59.

In order to simulate the self-generated magnetic fields, MHD solvers have been implemented into the code *DEC2D*. The induction equation, typically used to model the evolution of magnetic fields in ICF hot spot plasmas, which are quasi-neutral and fluid like (collisional) and in which the Ohm's law is applicable,[32] is implemented in *DEC2D*,

$$\partial_t \vec{B} = \underbrace{-\frac{\nabla n_e \times \nabla T_e}{n_e e}}_{\text{(i)}} + \underbrace{\nabla \times (\vec{v}_B \times \vec{B})}_{\text{(ii)}} + \underbrace{\nabla \times \left(\frac{\eta}{\mu_0} \nabla \times \vec{B}\right)}_{\text{(iii)}}. \quad (1)$$

Here, term (i) is the Biermann battery source term, term (ii) is the advection term, and term (iii) is the resistive diffusion term. All units in this paper are in SI and the temperature is in Joule.

Note that the Biermann battery term (i) is the only source term generating magnetic fields in the induction equation, and it causes self-generated magnetic fields to arise even when no initial magnetic fields are present.[33] This term is nonzero only in regions where the gradient in electron number density and the gradient in temperature are not aligned with each other. As shown in Fig. 3(a), this is true at the interface of the hot spot and shell in the case of deceleration-phase RTI. The gradients are also particularly large close to the tip of the spikes, producing the strongest magnetic fields there. Since in the 2D simulations the density and temperature gradients lie on the r–z plane, the Biermann-generated fields are perpendicular to the plane of the simulation. Furthermore, since the density gradients point in opposite directions on different sides of the spike, the magnetic fields alternate in sign.

The magnetic fields are advected according to the term (ii) in Eq. (1), where $\vec{v}_B$ is the sum of the fluid velocity and the Nernst velocity, $\vec{v}_B = \vec{v} + \vec{v}_N$. The Nernst velocity $\vec{v}_N$ is the sum of the component

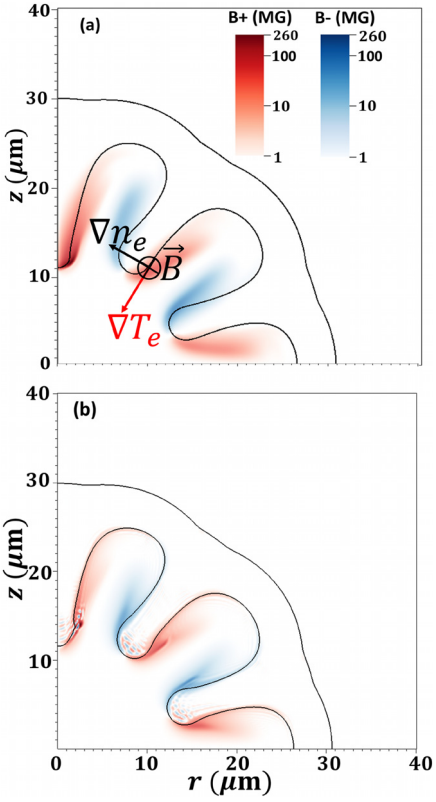

FIG. 3. The Biermann self-generated magnetic field, ∇n_e and ∇T_e, is shown at the interface between hot spot and shell at stagnation. The interface is perturbed nonlinearly due to the deceleration-phase RTI, initialized for $\ell = 10^*$. The shell boundary, represented using solid black lines, is determined using the contour $\rho = (1/e)\rho_{max1D}$ (from Ref. 7). Magnetic fields in the $+\hat{\phi}$ direction, i.e., into the page, are represented using red; fields in the $-\hat{\phi}$ direction, i.e., out of the page, are shown in blue. In all subsequent figures, the same convention for the shell boundary and the field representation is used. (a) Magnetic fields produced in a simulation with all MHD terms activated. (b) The case with only the resistive diffusion, term (iii) of Eq. (1), turned off in the simulation.

© Author(s) 2024

Version of Record at: https://doi.org/10.1063/5.0211922

perpendicular to the field $\vec{v}_{N\perp}$ and the cross $\vec{v}_{N\wedge}$ component (along isotherms) implemented using the Braginskii[34] formulation, given by

$$\vec{v}_{N\perp} = -\frac{\beta_\wedge}{\omega_e\tau_e}\frac{\tau_e}{m_e}\nabla T_e \propto -\frac{\beta_\wedge}{\omega_e\tau_e}\frac{T_e^{3/2}}{n_e}\nabla T_e, \tag{2a}$$

$$\vec{v}_{N\wedge} = -\frac{\beta_0-\beta_\perp}{\omega_e\tau_e}\frac{\tau_e}{m_e}(\hat{b}\times\nabla T_e) \propto -\frac{\beta_0-\beta_\perp}{\omega_e\tau_e}\frac{T_e^{3/2}}{n_e}(\hat{b}\times\nabla T_e), \tag{2b}$$

with the coefficients

$$\beta_\perp = \frac{\beta_1'\omega_e^2\tau_e^2+\beta_0'}{\omega_e^4\tau_e^4+\delta_1\omega_e^2\tau_e^2+\delta_0}, \quad \beta_\wedge = \frac{\omega_e\tau_e(\beta_1''\omega_e^2\tau_e^2+\beta_0'')}{\omega_e^4\tau_e^4+\delta_1\omega_e^2\tau_e^2+\delta_0}, \tag{2c}$$

$$\beta_0 = 0.711, \quad \beta_1' = 5.101, \quad \beta_0' = 2.681, \tag{2d}$$

$$\delta_1 = 14.79, \quad \delta_0 = 3.77, \quad \beta_1'' = 1.5, \quad \beta_0'' = 3.053. \tag{2e}$$

Here, $\vec{v}_{N\perp}$ is the component of the Nernst velocity in the direction perpendicular to the self-generated magnetic fields and $\vec{v}_{N\wedge}$ is the component perpendicular to both the magnetic field and the temperature gradient (i.e., along isotherms). The coefficients β and δ listed here (for completeness) are obtained from Braginskii.[34] Note that the Nernst velocity scales as $\vec{v}_N \propto -T^{3/2}n_e^{-1}\vec{\nabla}T_e$. Therefore, it pushes the self-generated magnetic fields against the temperature gradient toward the cold shell. The effect of the Nernst advection in the simulations will be discussed in Sec. III.

Term (iii) of Eq. (1) is the resistive diffusion term. Figure 3 demonstrates the effect of resistive diffusion on the self-generated fields in an implosion hot spot. Notice that the magnetic fields only diffuse marginally, such that their maximum value is lower. The overall magnetization is not significantly affected, and the magnetic fields still remain localized within the hot spot near the RTI spikes. This is due to the high magnetic Reynolds number at bang time, which is >15 in the magnetized regions. Thus, the magnetic fields are largely frozen-in to the plasma and are not dissipated significantly.

Plasma magnetization is depicted by the Hall parameter $\omega_e\tau_e$, in which ω_e is the electron gyrofrequency and τ_e is the electron collision time. Therefore, the Hall parameter measures the expected number of orbits between electron collisions. The Hall parameter $\omega_e\tau_e$ is given (in SI) by the following equation:[35]

$$\omega_e\tau_e = \frac{3(4\pi\varepsilon_0)^2}{4\sqrt{2\pi m_e}e^3}\frac{|\vec{B}|T_e^{3/2}}{n_e\ln\Lambda}\Bigg) = (9.44\times10^{50})\frac{BT_e^{3/2}}{n_e\ln\Lambda}, \tag{3}$$

where B is the magnetic field magnitude, T_e is the electron temperature (in J), n_e is the electron number density, and $\ln\Lambda$ is the Coulomb logarithm. *DEC2D* models only the deceleration phase of cryogenic implosions; by this time the outer plastic layer of the target is typically ablated off by laser heating, with only the deuterium–tritium (DT) shell and DT hot spot remaining. A $Z_{eff}=1$ is thus used throughout these simulations. Note that by virtue of the scaling $\omega_e\tau_e \propto T_e^{3/2}|B|n_e^{-1}$, the hot spot is easier to magnetize than the cold and dense plasma of the shell. The coefficients for heat transport (discussed in the following paragraph) and the Nernst velocity [in the term (ii) of Eq. (1)] depend on the Hall parameter,[34] hence $\omega_e\tau_e$ is used throughout this paper as a metric for plasma magnetization.

In addition to the induction equation, the magnetized heat transport is implemented according to Eq. (4). The heat transport for both the electrons and ions was implemented, although since ions were negligibly magnetized, the magnetized ion heat conduction has minimal impact on the fusion yield. Magnetized plasmas have suppressed heat conduction perpendicular to the magnetic fields.[34] Additionally, the Righi–Leduc transport causes heat to flow along the isotherms in magnetized plasmas. Thus, the previously isotropic heat flow equation is modified to include the effects of magnetization as

$$\vec{q} = -\kappa_\parallel\hat{b}(\hat{b}\cdot\nabla T_e) - \kappa_\perp\hat{b}\times(\nabla T_e\times\hat{b}) - \hat{b}\times\kappa_\wedge\nabla T_e, \tag{4}$$

in which $\hat{b}$ is the unit vector in the direction of the magnetic field and $\kappa_\parallel$, $\kappa_\perp$, and $\kappa_\wedge$ are the thermal conductivities. The coefficient $\kappa_\parallel$ is for the heat flow parallel to the magnetic fields, $\kappa_\perp$ is for the heat flow along the component of the temperature gradient perpendicular to the magnetic fields, and $\kappa_\wedge$ is for heat flow perpendicular to both the field and temperature gradient (i.e., along isotherms). Both $\kappa_\perp$ and $\kappa_\wedge$ depend on the plasma magnetization ($\omega_e\tau_e$), although $\kappa_\parallel$ remains unchanged. However, as the magnetic fields in *DEC2D* are generated perpendicularly to the plane of the simulation, only $\kappa_\perp$ and $\kappa_\wedge$ are used. The Braginskii formulation used[34] is given as follows:

$$\frac{\kappa_\perp}{\kappa_\parallel} = \frac{\gamma_1'\omega_e^2\tau_e^2+\gamma_0'}{\gamma_0\left[\omega_e^4\tau_e^4+\delta_1\omega_e^2\tau_e^2+\delta_0\right]}, \tag{5a}$$

$$\kappa_\wedge/\kappa_\perp = \frac{\omega_e\tau_e(\gamma_1''\omega_e^2\tau_e^2+\gamma_0'')}{\gamma_1'\omega_e^2\tau_e^2+\gamma_0'}, \tag{5b}$$

with the coefficients

$$\gamma_0 = 3.162, \quad \gamma_0' = 11.92, \quad \gamma_1' = 4.664, \quad \gamma_0'' = 21.67, \quad \gamma_1'' = 2.5, \quad \delta_0 = 3.77, \quad \delta_1 = 14.79. \tag{5c}$$

In summary, MHD solvers have been incorporated into the code *DEC2D* in order to model self-generated magnetic fields in the hot spot of ICF implosions. For brevity, only essential components of the solvers have been discussed here, with additional details to be made available in a forthcoming publication. In Sec. III, results on the effects of the self-generated magnetic field in Omega implosions for the three cases, low-mode, mid-mode, and multi-mode, will be discussed.

III. RESULTS

The magnetic field and Hall parameter at bang time for the three cases studied are shown in Fig. 4. Comparing the single mode cases first (both at the same yield, with YOC of 0.59), the peak magnetic field is lower for the $\ell = 2$ case, at 12 MG, than the $\ell = 10*$ case, at 256 MG. This clearly shows that a mid-mode perturbation produces higher magnetic fields than a low-mode asymmetry. The greater magnetic flux generation for larger ℓ is due to the greater curvatures of the RTI spikes, leading to larger $\nabla n_e \times \nabla T_e$, and thus larger Biermann magnetic fields.[17,32] Consequently, as can be seen in the right panel of Fig. 4, the Hall parameter also increases with the mode number ℓ. The maximum Hall parameter for the $\ell = 2$ case is 0.16 ($\omega_e\tau_e < 1$) whereas for the mid mode $\ell = 10*$ case it is 2.18 ($\omega_e\tau_e > 1$). This represents that there are local regions at the edge of the hot spot for the mid-modes where the plasma is strongly magnetized. For the multi-mode reconstruction of the 50 Gbar experiments, shown in the last row of Fig. 4, the peak magnetic field and Hall parameter are 200 MG and 1.46, respectively. Thus, while the mid-modes

© Author(s) 2024

Version of Record at: https://doi.org/10.1063/5.0211922

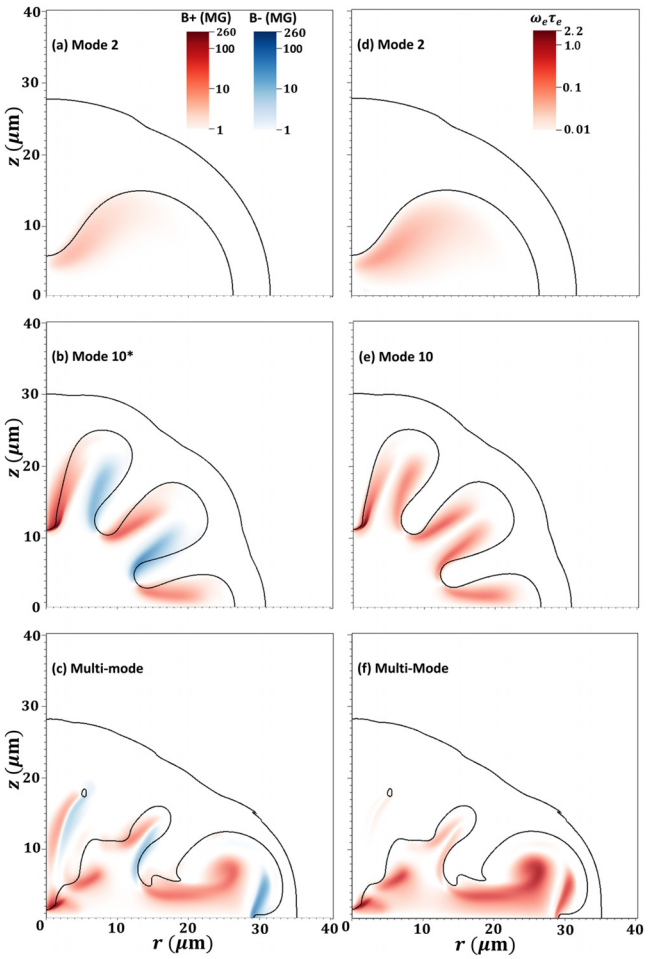

FIG. 4. The magnetic field (a)–(c) and Hall parameter (d)–(f) at bang time for low-mode $\ell = 2$ and mid-mode $\ell = 10^*$ asymmetry at YOC = 0.59 and the multi-mode reconstruction of the 50 Gbar shot 77 068 at YOC = 0.32. Since only half of the $\ell = 2$ spike is shown, only fields in the positive $\hat{\phi}$ direction are visible in this case.

generate most of the magnetic fields for the reconstructed Omega implosion, there is little contribution from the low modes.

At this point, we will discuss the effect of individual MHD terms [in Eqs. (1) and (4)] in order to both interpret and subsequently validate the role each term plays in the magnetic field dynamics.

A. Effect of individual MHD terms

In this section, the effects of individual MHD terms are analyzed. Table I shows the change in yield, the change in ion temperature (neutron-averaged), and the maximum Hall parameter for the mid-mode $\ell = 10*$ and multi-mode simulations. The mode 2 case is not discussed because the low magnetization ($\omega_e\tau_e < 1$) resulted in negligible differences overall due to the self-generated fields. Simulations with (1) Biermann term (only, i.e., Nernst and Righi–Leduc turned off), (2) Biermann and Nernst (i.e., Righi–Leduc turned off), and (3) Biermann, Nernst, and Righi–Leduc (i.e., all MHD terms activated) are shown. Note that fluid advection (excluding the Nernst advection), magnetic resistivity, and magnetized suppression of perpendicular heat transport ($\kappa_\perp$) are always kept activated in all these simulations. Only the terms listed previously have been deactivated in the simulations for this targeted study/validation of the role played by each of the key MHD terms.

1. Only Biermann battery

It can be seen in Table I that, with the Biermann term activated, but without the Nernst advection and the Righi–Leduc heat transport, the magnetic fields enhance the yield and ion temperature. The Biermann magnetic fields at the edge of the hot spot suppresses heat losses out of the hot spot. As can be seen from Fig. 5(b), the coefficient of thermal transport perpendicular to the magnetic field $\kappa_\perp$ decreases drastically by ≈90%, with $\omega_e\tau_e$ increasing from 0.1 to 2. However, for the Omega-scale implosions studied, although magnetization causes suppression of the thermal transport $\kappa_\perp$ perpendicular to the magnetic fields, the benefits (i.e., % increase) in yield and ion temperature are rather small, <1%. This increase is significantly lower than the 22.1% increase in yield for comparable (Biermann only) simulations at the NIF scale.[17] This will be discussed further in Sec. III B, which compares NIF and Omega.

2. The Nernst term

The Nernst velocity pushes the magnetic fields toward the cold shell. As shown in Fig. 6, when the Nernst term is deactivated in the simulations, the self-generated fields occupy more of the hot spot. When the Nernst advection is activated, the Nernst velocity $\vec{v}_N$ (shown using arrows) pushes the fields toward the cold and dense shell. The fields are therefore less effective in suppressing the heat losses. In Table I, the percent increase in yield and ion temperature is lower when the Nernst term is activated in addition to the Biermann term. However, the yield still increases with respect to the case without MHD, as the

TABLE I. The effect of individual MHD terms: (1) Biermann, (2) Biermann and Nernst, and (3) Biermann, Nernst, and Righi–Leduc.

		Yield/no MHD % increase	T_i % increase	Max $\omega_e\tau_e$
Mode 10*	(1) Biermann	0.57%	0.38%	0.91
	(2) Biermann + Nernst	0.09%	0.02%	1.63
	(3) Biermann + Nernst + Righi–Leduc	−4.14%	−0.71%	2.18
Multi-mode	(1) Biermann	0.76%	0.93%	1.87
	(2) Biermann + Nernst	0.25%	0.25%	1.45
	(3) Biermann + Nernst + Righi–Leduc	−2.42%	−1.09%	1.46

© Author(s) 2024

Version of Record at: https://doi.org/10.1063/5.0211922

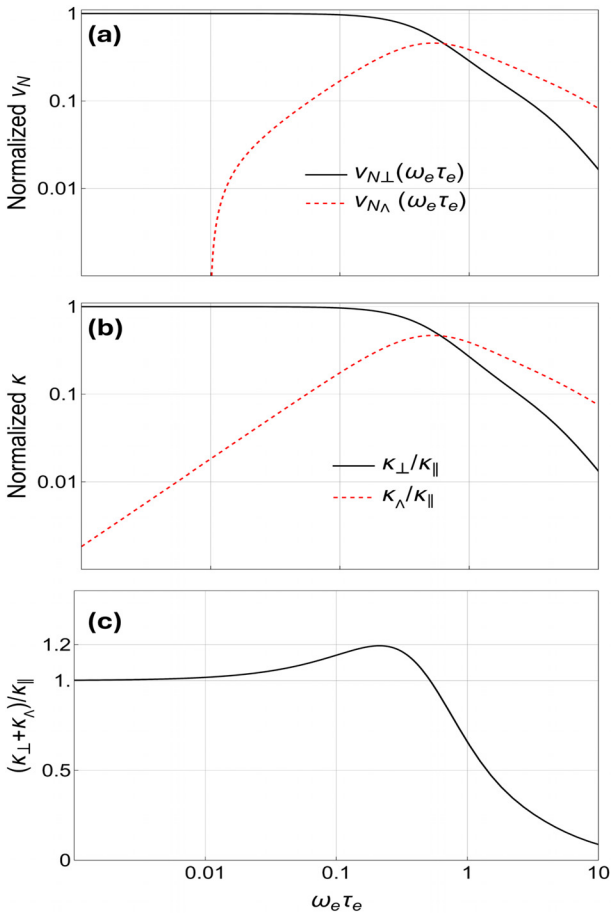

FIG. 5. Shows plots of the $\perp$ and $\wedge$ components of Nernst velocity (a), heat diffusion coefficients κ (b), and total magnetized heat flux (c), vs the Hall parameter ($\omega_e\tau_e$). In (a), the Nernst velocity is normalized to $v_{N\perp}(\omega_e\tau_e = 0)$. In (b), the κ coefficients are normalized to $\kappa_\parallel$, i.e. the unmagnetized heat flow.

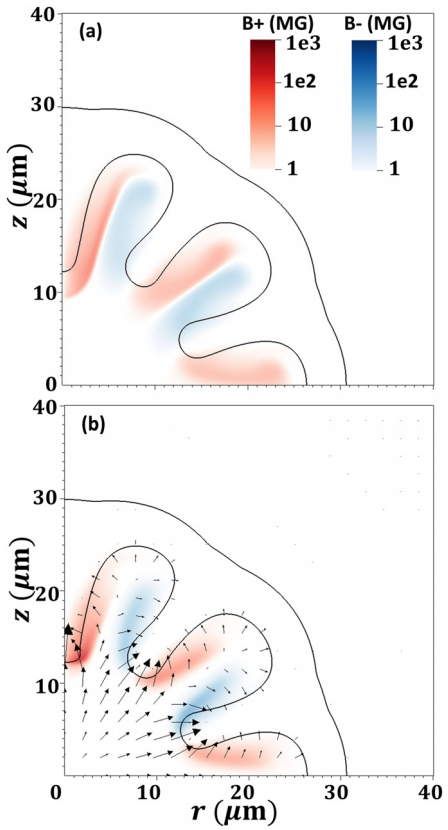

FIG. 6. The effect of Nernst advection is shown via comparison between simulations: (a) with the Nernst advection turned off and (b) with the Nernst advection turned on. The Nernst velocity $\vec{v}_N$ is represented using arrows.

perpendicular heat transport is still suppressed slightly by these magnetic fields, which pile up at the edge of the hot spot due to the Nernst advection.

The Nernst velocity, in analogy with anisotropic thermal conduction, also has an anisotropy between components in the direction perpendicular to the magnetic field ($v_{N\perp}$) and in the direction of the isotherms ($v_{N\wedge}$).[34] The $v_{N\perp}$ advects the magnetic fields antiparallel to the temperature gradients, from regions of higher temperature to regions of lower temperature. $v_{N\wedge}$ advects fields along isotherms, pushing the magnetic field along the edge of the RTI spikes toward the cooler bubbles. The Nernst velocity components $v_{N\perp}$ and $v_{N\wedge}$ have different dependence on the electron Hall parameter, as shown in Fig. 5(a). The component $v_{N\perp}$ decreases significantly with increasing Hall parameter, decreasing to 90% for $\omega_e\tau_e \sim 2$. This is not the case for $v_{N\wedge}$, which goes from being small to being larger than $v_{N\perp}$ as the Hall parameter increases from 0.1 to 2. However, since the hot spot is mostly unmagnetized ($\omega_e\tau_e < 1$, except for a few local regions near the tip of the spikes) for the Omega implosions, $v_{N\wedge}$ plays only a modest role. Overall, the Nernst velocity predominantly pushes the magnetic fields against the temperature gradients toward the colder shell.

3. The Righi–Leduc term

As shown in Table I, for both the mid-mode and multi-mode cases, including the Righi–Leduc term in the simulations produces a net drop in the fusion yield and a drop in the ion-temperature (below the no MHD case). For the mid-mode $\ell = 10*$ simulation considered, the drop in yield and ion-temperature is by 4.14% and 0.71%, respectively. This outcome contradicts the assertion made in the recent paper,[16] where it was stated that the Righi–Leduc term has no effect on the hot spot heat loss rate, as heat is moved along the isotherms. This intuition fails to incorporate the dynamic effects of the inclusion of magnetized heat flows both along temperature gradients and along isotherms for the spatially localized Biermann fields and calls for MHD simulations of ICF implosions. Figure 7 shows that the Righi–Leduc term transports heat from the central regions of the hot spot, along the isotherms, to the unmagnetized portions of the RTI bubbles. Though the Righi–Leduc term directs heat along isotherms, and therefore by itself cannot directly cause a net heat loss, it plays the important role of funneling heat into the bubbles, i.e., away from the magnetized regions

© Author(s) 2024

Version of Record at: https://doi.org/10.1063/5.0211922

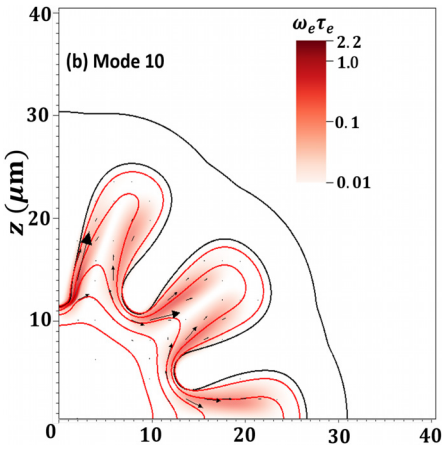

FIG. 7. The Righi–Leduc heat transport in the hot spot is shown. The red lines show contours of constant temperature, and the black arrows represent the Righi–Leduc heat flux. The Hall parameter is depicted using a red shade. The plot is for the mode 10* case at bang time.

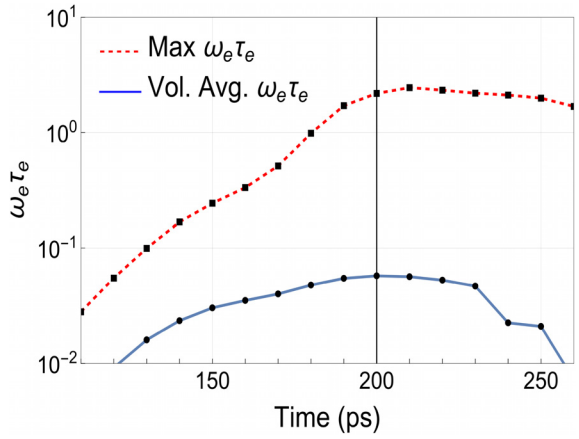

FIG. 8. Time evolution of the hot spot magnetization Hall parameter ($\omega_e\tau_e$) around bang time (200 ps since start of the deceleration-phase) for the mode 10* simulation.

close to the spike tips. The heat is then lost from the bubbles to the cold shell (across isotherms) because the unmagnetized bubbles allow uninhibited perpendicular heat transport. Thus, there is a net heat loss aided by the Righi–Leduc effect. This result may seem surprising, as intuitively, magnetizing plasma causes the heat flux to decrease. However, as demonstrated in Fig. 5(c), for $0.01 < \omega_e\tau_e < 0.5$, the total magnetized thermal transport coefficient, i.e., including both the heat flux across gradients and along isotherms, exceeds the unmagnetized thermal transport coefficient by ≈20%. In this Hall parameter regime, which corresponds to the Omega implosions considered, magnetization can potentially result in higher heat losses. Figure 8 shows a comparison of the hot spot volume-averaged Hall parameter and the peak Hall parameter, demonstrating that although the maximum Hall parameter is ∼2, the volume-averaged $\omega_e\tau_e \sim 0.1$. This implies that most of the heat flow in the hot spot is in the magnetization regime in which the heat flux is increased.

B. The effect of self-generated magnetic fields on Omega implosion yield and comparison with indirect-drive NIF implosions

The self-generated magnetic fields cause a drop in fusion yield and ion temperature by 2.42% and 1.09%, respectively, for the reconstructed (multi-mode) 50 Gbar Omega implosion, as shown in Table II. The table lists results for the three perturbation cases studied and the symmetric (clean) case; the symmetric case lacks perturbations and magnetic fields. For all perturbation cases, the yield-over-clean (YOC) and neutron-averaged ion temperatures with MHD deactivated are shown in the first two columns. The next two columns list the percent change in the yield and ion temperature with the inclusion of self-generated magnetic fields (with all MHD terms activated). Notice that although all cases result in a decrease in the yield and ion temperature, the drop in both yield and ion temperature is rather small for the Omega-scale implosions. The yield drop is within the 5% error in yield measurement and the neutron-averaged ion temperature is within the 8% (300 eV) error in measurements (the error estimates are obtained from Table I of Ref. 19). Table II also lists the minimum ratio of $\kappa_\perp/\kappa_\parallel$ and the maximum ratio of $\kappa_\wedge/\kappa_\perp$. The former ($\kappa_\perp/\kappa_\parallel$ Min.) represents the maximum suppression of the perpendicular heat transport due to magnetization, in which $\kappa_\parallel$ is the unmodified heat transport. Considering the multi-mode case, the ratio is 0.17, which is comparable to 0.10 for a multi-mode NIF simulation listed in Table I of Ref. 17. Comparing the minimum of $\kappa_\perp/\kappa_\parallel$ for the low mode $\ell = 2$ and the mid-mode $\ell = 10*$, it is seen that the suppression of heat transport due to magnetization increases (i.e., $\kappa_\perp/\kappa_\parallel$ min. decreases) with the mode number ℓ. This is due to the fact that the magnetization (max. $\omega_e\tau_e$) also increases with ℓ (in agreement with Ref. 32). The last column of Table II lists the maximum ratio of the Righi–Leduc diffusion coefficient $\kappa_\wedge$ to the perpendicular diffusion coefficient, $\kappa_\wedge/\kappa_\perp$. This parameter represents the relative significance of the Righi–Leduc

TABLE II. Yield and thermal transport coefficient ratios at bang time for different modes. Ion temperatures are neutron-averaged. The symmetric yield was 1.70×10^{14}.

			With MHD activated				
Mode	YOC	T_i (keV)	ΔYield	ΔT_i	Max $\omega_e\tau_e$	$\kappa_\perp/\kappa_\parallel$ Min	$\kappa_\wedge/\kappa_\perp$ Max
Symmetric	1	3.89	NA	NA	NA	NA	NA
Mode 2	0.59	3.80	−0.36%	−0.15%	0.16	0.92	0.29
Mode 10*	0.59	3.92	−4.14%	−0.71%	2.18	0.11	2.15
Multi-mode	0.32	3.83	−2.42%	−1.09%	1.46	0.17	1.80

© Author(s) 2024

Version of Record at: https://doi.org/10.1063/5.0211922

effect to the perpendicular heat flow suppression. For the $\ell = 2$ case, this parameter is much lower than the $\ell = 10*$ case, showing that the Righi–Leduc effect increases for mid-modes. The multi-mode case, which is a combination of the low and mid-modes, also shows a significant Righi–Leduc effect.

For the Omega-scale simulations, the change in yield is $\approx 5\times$ lower (for the realistic reconstructed direct-drive 50 Gbar implosions) compared to indirect-drive NIF simulations. The change in yield for Omega-scale (this work) and NIF-scale (from Ref. 17) simulations is listed in Table III. Notice that although the percent changes are lower in magnitude at Omega, the trend in yield is in agreement with the NIF studies, i.e., (1) the Biermann-only simulation causes yield increase, (2) Biermann + Nernst reduces boost in yield, and (3) Biermann + Nernst + Righi–Leduc causes yield drop below the no-MHD case. Beyond the agreement in trend, it is important to note that there are limitations in conducting a quantitative comparison between the two cases. This is because they are conducted for different implosion parameters (direct-drive at Omega vs indirect-drive at NIF), and conducted using different simulation codes. Hence, we proceed with caution to outline the differences and discuss probable causes. Considering the simulations with the (1) Biermann term only (i.e., with suppressed $\kappa_\perp$ only due to magnetization), the increase in yield at NIF scale is $\approx 28\times$ that of Omega, listed in Table III. This shows that, at NIF scale, the impact of the field on the fusion yield (even prior to the inclusion of Nernst and Righi–Leduc terms) is already significantly larger than at Omega. However, the peak magnetic field (> 100 MG) and Hall parameter ($\omega_e > 1$) are almost the same between the NIF[17] and Omega (this work). For the (2) Biermann + Nernst simulation, the percent change in Omega yield is also smaller than in the NIF simulation. Considering the simulations with all MHD included (3), activation of the Righi–Leduc term alone causes the yield to drop by -2.7% at Omega compared to a drop by -25.8% at NIF. Thus, the Righi–Leduc term is the dominant MHD term (in terms of its effect on yield) for both Omega and NIF scales. It is possible that the relatively smaller change in yield for Omega scale is because of either or all of the following: (1) The perturbation modes used to degrade the NIF and Omega simulations are different. The NIF-scale simulation used low- and high-mode (possibly $\ell \sim 40$–200) asymmetries of the hot spot to degrade the implosion.[17] It is possible that the short-scale fluctuations caused by the high modes used in the NIF studies generated an envelope of magnetized plasma at the edge of the hot spot. Therefore, although the peak magnetic field is comparable between the NIF and Omega, the suppression of perpendicular thermal transport within the magnetized envelope produces higher changes to the yield. By contrast, for the reconstructed Omega simulation in this work, mid-modes (corresponding to the laser beam modes) were used instead of high modes. This was based on a simultaneous reconstruction of all stagnation observables.[19] The mid-modes, unlike the short-scale high-modes, produced local regions of magnetization instead of a magnetized plasma envelope at the hot spot edge. This could possibly explain why, for the Biermann-only case (1) in Table III, the NIF implosion had yield increases of 22.1% from the Biermann fields alone, in contrast to the 0.8% increase found in this analysis. (2) For the larger NIF-scale targets, the self-generated magnetic fields occupy a greater volume and exist for a longer period of time. Figure 8 shows time evolution of the maximum Hall parameter and the volume-averaged Hall parameter in the hot spot as a function of time. Though the maximum $\omega_e\tau_e > 1$, the volume-averaged $\omega_e\tau_e \sim 0.1$. Thus, most of the hot spot volume is unmagnetized, with an average Hall parameter of around 0.1. Therefore, due to the localized nature of magnetized regions, the effect of the self-generated magnetic fields on the Omega yield is small. (3) For the NIF-scale simulations, the yield is amplified due to alpha heating. Since alpha heating is proportional to T_i^4, small changes in temperature due to the fields cause significant changes to the alpha heating and consequently the fusion yield. As alpha heating was always active for the NIF simulations,[17] the effects of alpha heating on these self-generated magnetic fields could not be isolated, and therefore the smaller changes in yield at Omega can be due to the lack of alpha heating at the Omega scale.

TABLE III. A comparison of the change in yield due to self-generated magnetic fields between direct-drive Omega and indirect-drive NIF implosions.[17] The effect of individual MHD terms on the yield: (1) Biermann, (2) Biermann and Nernst, and (3) Biermann, Nernst, and Righi–Leduc is shown.

	Omega	NIF
(1) Biermann	0.8%	22.1%
(2) Biermann + Nernst	0.3%	14.2%
(3) Biermann + Nernst + Righi–Leduc	−2.4%	−11.6%

IV. CONCLUSION

In this work, a quantitative estimate of the effect of the self-generated Biermann magnetic fields on yield and ion temperature for direct-drive cryogenic Omega implosions has been provided. This estimation is essential because direct measurements of the hot spot fields are not available. It is found that Biermann self-generated magnetic fields up to $\approx$200–250 MG and Hall parameter up to ≈ 2 are produced during the stagnation phase of direct-drive Omega implosions. The magnetic fields produce a drop of 2.4% in the fusion yield and 1% drop in the ion temperature. Reconstructed simulations of the 50 Gbar implosions, with all the stagnation measurements reproduced simultaneously by a combination of mid- and low-mode asymmetries as degradation mechanisms, were used in obtaining the estimates.[19]

It is found that the magnetic fields cause a decrease in yield due to the Righi–Leduc heat loss mechanism, which surpasses any benefits from heat-flow suppression due to magnetization. The Righi–Leduc term funnels heat flux along isotherms from the central regions of the hot spot (at the vicinity of the RTI spikes where the plasma is magnetized by the self-generated fields) into the unmagnetized bubble regions. The heat flux then diffuses to the shell, thus resulting in hot spot heat loss, and consequently a drop in the fusion yield.

For direct-drive Omega implosions, since the laser drive can imprint mid-modes due to the laser beam geometry and cross-beam energy transport, and low modes can arise from target offsets, both these modes and their effects have been modeled in this work. It is found that mid-modes generate more magnetic flux than low modes, with $\omega_e\tau_e \sim 2.18$ at bang time for mid-modes compared to $\omega_e\tau_e \sim 0.16$ for low modes. As a result, mid-modes also result in a higher drop in yield than low modes.

It is important to note that both direct-drive Omega-scale implosions and indirect-drive NIF-scale implosions produce similar estimates for the magnetic field strength, and both show a decrease in fusion yield with the Righi–Leduc transport as the loss mechanism.

© Author(s) 2024

Version of Record at: https://doi.org/10.1063/5.0211922

Maximum self-generated magnetic fields of 200 MG and maximum Hall parameters $\omega_e\tau_e \sim 1.5$ are simulated for the multi-mode, comparable to the maximum magnetic fields for indirect-drive NIF-scale implosions. However, the yield degradation at Omega is lower by $\approx 5\times$ compared to indirect-drive NIF implosions. Thus, the degradation in yield and ion temperatures caused by self-generated magnetic fields in the hot spot is modest for direct-drive sub-ignition scale Omega implosions.

ACKNOWLEDGMENTS

This work was supported by a sub-award made by the Laboratory for Laser Energetics, University of Rochester, SUB00000056/GR530167/AWD00002510, under the Department of Energy, National Nuclear Security Administration Grant No. DE-NA0003856. The simulations reported in this paper were conducted using the high-performing cluster, Caviness, at the University of Delaware. The authors would also like to thank the anonymous reviewers for their feedback, which have helped accentuate the key findings of this paper.

AUTHOR DECLARATIONS

Conflict of Interest

The authors have no conflicts to disclose.

Author Contributions

C. A. Frank: Conceptualization (equal); Formal analysis (equal); Investigation (equal); Methodology (equal); Writing – original draft (equal). **A. Bose:** Conceptualization (lead); Funding acquisition (lead); Investigation (equal); Methodology (equal); Resources (lead); Supervision (lead); Validation (equal); Writing – original draft (equal); Writing – review & editing (lead).

DATA AVAILABILITY

The data that support the findings of this study are available from the corresponding author upon reasonable request.

REFERENCES

[1]S. Atzeni and J. Meyer-ter Vehn, *The Physics of Inertial Fusion: Beam Plasma Interaction, Hydrodynamics, Hot Dense Matter*, 1st ed. (Oxford University Press, 2009).
[2]F. Hattori, H. Takabe, and K. Mima, "Rayleigh–Taylor instability in a spherically stagnating system," Phys. Fluids **29**(5), 1719–1724 (1986).
[3]V. Lobatchev and R. Betti, "Ablative stabilization of the deceleration phase Rayleigh-Taylor instability," Phys. Rev. Lett. **85**, 4522–4525 (2000).
[4]R. Betti, M. Umansky, V. Lobatchev, V. N. Goncharov, and R. L. McCrory, "Hot-spot dynamics and deceleration-phase Rayleigh–Taylor instability of imploding inertial confinement fusion capsules," Phys. Plasmas **8**(12), 5257–5267 (2001).
[5]R. Kishony and D. Shvarts, "Ignition condition and gain prediction for perturbed inertial confinement fusion targets," Phys. Plasmas **8**(11), 4925–4936 (2001).
[6]R. Betti, K. Anderson, V. N. Goncharov, R. L. McCrory, D. D. Meyerhofer, S. Skupsky, and R. P. J. Town, "Deceleration phase of inertial confinement fusion implosions," Phys. Plasmas **9**, 2277 (2002).
[7]A. Bose, R. Betti, D. Shvarts, and K. M. Woo, "The physics of long- and intermediate-wavelength asymmetries of the hot spot: Compression hydrodynamics and energetics," Phys. Plasmas **24**, 102704 (2017).
[8]J. R. Rygg, F. H. Séguin, C. K. Li, J. A. Frenje, M. J.-E. Manuel, R. D. Petrasso, R. Betti, J. A. Delettrez, O. V. Gotchev, J. P. Knauer, D. D. Meyerhofer, F. J. Marshall, C. Stoeckl, and W. Theobald, "Proton radiography of inertial fusion implosions," Science **319**(5867), 1223–1225 (2008).
[9]C. K. Li, F. H. Séguin, J. R. Rygg, J. A. Frenje, M. Manuel, R. D. Petrasso, R. Betti, J. Delettrez, J. P. Knauer, F. Marshall, D. D. Meyerhofer, D. Shvarts, V. A. Smalyuk, C. Stoeckl, O. L. Landen, R. P. J. Town, C. A. Back, and J. D. Kilkenny, "Monoenergetic-proton-radiography measurements of implosion dynamics in direct-drive inertial-confinement fusion," Phys. Rev. Lett. **100**, 225001 (2008).
[10]C. K. Li, F. H. Séguin, J. A. Frenje, M. Manuel, D. Casey, N. Sinenian, R. D. Petrasso, P. A. Amendt, O. L. Landen, J. R. Rygg, R. P. J. Town, R. Betti, J. Delettrez, J. P. Knauer, F. Marshall, D. D. Meyerhofer, T. C. Sangster, D. Shvarts, V. A. Smalyuk, J. M. Soures, C. A. Back, J. D. Kilkenny, and A. Nikroo, "Proton radiography of dynamic electric and magnetic fields in laser-produced high-energy-density plasmas," Phys. Plasmas **16**(5), 056304 (2009).
[11]M. J.-E. Manuel, C. K. Li, F. H. Séguin, J. Frenje, D. T. Casey, R. D. Petrasso, S. X. Hu, R. Betti, J. D. Hager, D. D. Meyerhofer, and V. A. Smalyuk, "First measurements of Rayleigh-Taylor-induced magnetic fields in laser-produced plasmas," Phys. Rev. Lett. **108**, 255006 (2012).
[12]L. Gao, P. M. Nilson, I. V. Igumenschev, S. X. Hu, J. R. Davies, C. Stoeckl, M. G. Haines, D. H. Froula, R. Betti, and D. D. Meyerhofer, "Magnetic field generation by the Rayleigh-Taylor instability in laser-driven planar plastic targets," Phys. Rev. Lett. **109**, 115001 (2012).
[13]I. V. Igumenshchev, A. B. Zylstra, C. K. Li, P. M. Nilson, V. N. Goncharov, and R. D. Petrasso, "Self-generated magnetic fields in direct-drive implosion experiments," Phys. Plasmas **21**, 062707 (2014).
[14]B. Srinivasan, G. Dimonte, and X.-Z. Tang, "Magnetic field generation in Rayleigh-Taylor unstable inertial confinement fusion plasmas," Phys. Rev. Lett. **108**, 165002 (2012).
[15]B. Srinivasan and X.-Z. Tang, "Mechanism for magnetic field generation and growth in Rayleigh-Taylor unstable inertial confinement fusion plasmas," Phys. Plasmas **19**, 082703 (2012).
[16]J. D. Sadler, C. A. Walsh, Y. Zhou, and H. Li, "Role of self-generated magnetic fields in the inertial fusion ignition threshold," Phys. Plasmas **29**(7), 072701 (2022).
[17]C. A. Walsh, J. P. Chittenden, K. McGlinchey, N. P. L. Niasse, and B. D. Appelbe, "Self-generated magnetic fields in the stagnation phase of indirect-drive implosions on the National Ignition Facility," Phys. Rev. Lett. **118**, 155001 (2017).
[18]A. Hata, K. Mima, A. Sunahara, H. Nagatomo, and A. Nishiguchi, "Dynamics of self-generated magnetic fields in stagnation phase and their effects on hot spark formation," Plasma Fusion Res. **1**, 020 (2006).
[19]A. Bose, R. Betti, D. Mangino, K. M. Woo, D. Patel, A. R. Christopherson, V. Gopalaswamy, O. M. Mannion, S. P. Regan, V. N. Goncharov *et al.*, "Analysis of trends in experimental observables: Reconstruction of the implosion dynamics and implications for fusion yield extrapolation for direct-drive cryogenic targets on omega," Phys. Plasmas **25**(6), 062701 (2018).
[20]D. H. Edgell, R. K. Follett, I. V. Igumenshchev, J. F. Myatt, J. G. Shaw, and D. H. Froula, "Mitigation of cross-beam energy transfer in symmetric implosions on omega using wavelength detuning," Phys. Plasmas **24**, 062706 (2017).
[21]D. H. Edgell, P. B. Radha, J. Katz, A. Shvydky, D. Turnbull, and D. H. Froula, "Nonuniform absorption and scattered light in direct-drive implosions driven by polarization smoothing," Phys. Rev. Lett. **127**, 075001 (2021).
[22]S. P. Regan, V. N. Goncharov, I. V. Igumenshchev, T. C. Sangster, R. Betti, A. Bose, T. R. Boehly, M. J. Bonino, E. M. Campbell, D. Cao, T. J. B. Collins, R. S. Craxton, A. K. Davis, J. A. Delettrez, D. H. Edgell, R. Epstein, C. J. Forrest, J. A. Frenje, D. H. Froula, M. Gatu Johnson, V. Yu. Glebov, D. R. Harding, M. Hohenberger, S. X. Hu, D. Jacobs-Perkins, R. Janezic, M. Karasik, R. L. Keck, J. H. Kelly, T. J. Kessler, J. P. Knauer, T. Z. Kosc, S. J. Loucks, J. A. Marozas, F. J. Marshall, R. L. McCrory, P. W. McKenty, D. D. Meyerhofer, D. T. Michel, J. F. Myatt, S. P. Obenschain, R. D. Petrasso, P. B. Radha, B. Rice, M. J. Rosenberg, A. J. Schmitt, M. J. Schmitt, W. Seka, W. T. Shmayda, M. J. Shoup, A. Shvydky, S. Skupsky, A. A. Solodov, C. Stoeckl, W. Theobald, J. Ulreich, M. D. Wittman, K. M. Woo, B. Yaakobi, and J. D. Zuegel, "Demonstration of fuel hot-spot pressure in excess of 50 Gbar for direct-drive, layered deuterium-tritium implosions on omega," Phys. Rev. Lett. **117**, 025001 (2016).

© Author(s) 2024

Version of Record at: https://doi.org/10.1063/5.0211922

[23]A. Bose, K. M. Woo, R. Betti, E. M. Campbell, D. Mangino, A. R. Christopherson, R. L. McCrory, R. Nora, S. P. Regan, V. N. Goncharov, T. C. Sangster, C. J. Forrest, J. Frenje, M. Gatu Johnson, V. Y. Glebov, J. P. Knauer, F. J. Marshall, C. Stoeckl, and W. Theobald, "Core conditions for alpha heating attained in direct-drive inertial confinement fusion," Phys. Rev. E **94**, 011201 (2016).
[24]K. M. Woo *et al.*, "Effects of residual kinetic energy on yield degradation and ion temperature asymmetries in inertial confinement fusion implosions," Phys. Plasma **25**, 052704 (2018).
[25]J. Delettrez, R. Epstein, M. C. Richardson, P. A. Jaanimagi, and B. L. Henke, "Effect of laser illumination nonuniformity on the analysis of time-resolved x-ray measurements in uv spherical transport experiments," Phys. Rev. A **36**, 3926–3934 (1987).
[26]I. V. Igumenshchev, W. Seka, D. H. Edgell, D. T. Michel, D. H. Froula, V. N. Goncharov, R. S. Craxton, L. Divol, R. Epstein, R. Follett, J. H. Kelly, T. Z. Kosc, A. V. Maximov, R. L. McCrory, D. D. Meyerhofer, P. Michel, J. F. Myatt, T. C. Sangster, A. Shvydky, S. Skupsky, and C. Stoeckl, "Crossed-beam energy transfer in direct-drive implosions," Phys. Plasmas **19**, 056314 (2012).
[27]V. N. Goncharov, T. C. Sangster, P. B. Radha, R. Betti, T. R. Boehly, T. J. B. Collins, R. S. Craxton, J. A. Delettrez, R. Epstein, V. Y. Glebov, S. X. Hu, I. V. Igumenshchev, J. P. Knauer, S. J. Loucks, J. A. Marozas, F. J. Marshall, R. L. McCrory, P. W. McKenty, D. D. Meyerhofer, S. P. Regan, W. Seka, S. Skupsky, V. A. Smalyuk, J. M. Soures, C. Stoeckl, D. Shvarts, J. A. Frenje, R. D. Petrasso, C. K. Li, F. Seguin, W. Manheimer, and D. G. Colombant, "Performance of direct-drive cryogenic targets on OMEGA," Phys. Plasmas **15**(5), 056310 (2008).
[28]K. Anderson, R. Betti, and T. A. Gardiner, "Two-dimensional computational model of energy gain in NIF capsules," Bull. Am. Phys. Soc. **46**, 280 (2001).
[29]A. Bose, K. M. Woo, R. Nora, and R. Betti, "Hydrodynamic scaling of the deceleration-phase Rayleigh–Taylor instability," Phys. Plasmas **22**(7), 072702 (2015).
[30]A. Bose, "Direct drive inertial confinement fusion: Analysis of the implosion core," Ph.D. thesis (University of Rochester, 2017).
[31]K. M. Woo, "The influence of three dimensional effects on the core dynamics and nuclear measurements of inertial fusion implosions," Ph.D. thesis (University of Rochester, 2019).
[32]C. A. Walsh and D. S. Clark, "Biermann battery magnetic fields in ICF capsules: Total magnetic flux generation," Phys. Plasmas **28**, 092705 (2021).
[33]L. Biermann, "Über den Ursprung der Magnetfelder auf Sternen und im interstellaren Raum (miteinem Anhang von A. Schlüter)," Z. Nat. A **5**, 65 (1950).
[34]S. I. Braginskii, "Transport processes in plasma," Rev. Plasma Phys. **1**, 205–311 (1965).
[35]A. S. Richardson, "2019 NRL Plasma Formulary" (2019), see https://library.psfc.mit.edu/catalog/online_pubs/NRL_FORMULARY_19.pdf.

© Author(s) 2024